3 Biotech (2026) 16:202
https://doi.org/10.1007/s13205-026-04838-4

ORIGINAL ARTICLE

Electro- and photo-catalytic performance of sono-assisted biogenic gold nanoparticles towards industrial contaminant: malachite green

Merina Paul Das[1] · **Jayabrata Das**[2]

Received: 6 February 2026 / Accepted: 22 April 2026

Abstract

The present study demonstrates a facile and rapid method for green synthesis of gold nanoparticles (AuNPs). This method utilizes an unreported *Citrus grandis* peel extract as an eco-friendly reducing and stabilizing agent in a sonocatalysis process under the influence of ultrasonics waves (40 kHz at 50 W). The sono-assisted synthesis of AuNPs took only 5 min at 37 °C. The formation of AuNPs was confirmed by surface plasmon resonance (SPR) band located at 561 nm and the morphology, crystallinity, purity, and stability were characterized by FESEM, TEM, XRD, EDX and zeta potential analysis. The as-synthesized AuNPs was then investigated for the electrocatalysis and photocatalysis against an industrial contaminant malachite green (MG). DPV analysis of AuNPs modified glassy carbon electrode (AuNPs/GCE) shows a moderate dynamic range over 1 to 40 µM for MG with a limit of detection (LoD) of 298 nM and a sensitivity of 0.373 µA μM^{-1} cm^{-2}. Further, AuNPs as a heterogeneous catalyst exhibits a photocatalytic reduction of MG in the presence of $NaBH_4$. The reduction of MG follows first-order kinetic model with an estimated apparent reduction rate of 4.51×10^{-2} min^{-1}. This result highlights the potential use of green synthesized AuNPs in wastewater management.

Keywords *Citrus grandis* · Gold nanoparticles · Malachite green · Electrochemical detection · Photocatalytic reduction · Sonochemistry

Introduction

The intrinsic optoelectronic and biocompatible properties of gold nanoparticles (AuNPs) make them a magnificent resource to be utilized for applications in diverse biomedical engineering, catalysis, electronic devices, etc. (Choudhary et al. 2017; Das and Velusamy 2014). These properties can easily be tuned by controlling the synthesis reaction. Concern of biocompatibility, it is of considerable interest to develop green chemistry approaches for the synthesis of AuNPs, which is rapid and cost-effective. Plant extracts or microorganisms mediated biosynthetic reaction of NPs often encounters with low concentration of available bioreductants and elevated temperature for a higher reaction rate (Nojedehi et al. 2018). Chemical synthesis of metal NPs is faster and can be carried out at room temperature, but the use of harsh and toxic chemicals including $NaBH_4$, mercaptonol, sodium dodecyl sulfate, etc. is subject of concern (Satpathy and Manikandan 2020). In general, green-physical methods like gamma-, microwave-, UV-irradiation, and sono-electrochemistry are being considered for the synthesis of AuNPs (Elsupikhe et al. 2015). Nevertheless, all these procedures are slow and expensive. As an alternate, ultrasonication is a remarkable and interesting option owing to its simplicity and accelerating the various synthetic reactions (Nasef et al. 2016).

The sonochemistry assisted synthesis of AuNPs is relying on the dissociation of precursor by high power ultrasonic irradiation (20 kHz to 10 mHz). During sonolysis, all the chemical consequences at the nucleation site are originated from an acoustic cavitation force due to collapse of the microbubbles in the rarefying phase. Eventually this cavitation generates intense local heating (hot spots of ≈ 5000 °C), ultrasonic energy (frequency ≥ 20 kHz),

✉ Jayabrata Das
jaydas09@gmail.com

[1] Department of Biochemistry, School of Life Sciences, Vels Institute of Science, Technology and Advanced Studies, Chennai 600117, Tamil Nadu, India

[2] Department of Biotechnology, School of Bioengineering, SRM Institute of Science and Technology, Kattankulathur, Chennai 603 203, Tamil Nadu, India

Published online: 19 May 2026

high pressure (≈1000 atm) and rapid heating and cooling rates (above 1010 K/s) leading to formation of metal atoms and subsequently agglomerate to form nanoparticles (Shirazi and Akhbar 2016). These characteristics of cavitation forces are mostly responsible for size and shape specific nanoparticle synthesis (Patil and Bhanage 2016). Vasantharaj et al. reported that acoustic cavitation forces during ultrasonic irradiation affect the surface structure of the AuNPs and prevent its aggregation in a solution, resulting a more stable colloidal dispersion that are often unavailable by conventional methods (Vasantharaj et al. 2018). However, several reports are also available in the literature to prefer the stabilizing agent like sodium dodecyl sulfate, polyethylene glycol, polyvinylpyrolidone etc. along with ultrasonic irradiation to control the agglomeration of the nanoparticles (Sáez and Mason 2009; Bhosale et al. 2017). Previously, biomaterials such as starch (Kumar et al. 2018), κ-carrageenan (Wan et al. 2021), sodium citrate (Ahmad et al. 2023; Poklepovich-Caride et al. 2022) etc. were used along with ultrasonic waves to govern the particle nucleation and growth process have been reported. Only a few plant sources including corncob-AgNPs (Karadirek and Okkay 2019), *Hibiscus rosa-sinensis*-CuNPs (Dinesh et al. 2020), fenugreek-Fe_2O_3NPs & AgNPs (Deshmukh et al. 2019), geranium-AuNPs (Franco-Romano et al. 2014), *Prosopis farcta*-PtNPs (Jameel et al. 2020), and palm oil fronds-AuNPs (Usman et al. 2020) have been documented for sono-assisted green synthesis of metallic nanoparticles in the literature.

Motivated by its good catalytic properties of AuNPs, the present work is further designed to explore the as-synthesized AuNPs for electro- and photo-catalysis against a model dye Malachite green (MG); a toxic and carcinogenic triphenylmethane dye. This contaminant is widely used in textile, leather, paper industries and subsequently pollutes the water systems. Progressive accumulation of the dye in animal and human bodies causes severe effects like skin irritation, carcinogenicity, etc. and reported to be a priority chemical according to Food and Drug Administration (Vergis et al. 2018). Currently, detection of MG can be precisely carried out with flow injection analysis, high performance liquid chromatography coupled with mass spectrometry, electrochemiluminescence, and surface enhanced Raman spectroscopy etc. (Sacara et al. 2017a, b). Woefully, all these techniques require an expensive and sophisticated instrument and thus not suitable for field applications. In this context, as-synthesized AuNPs based electrochemical sensor has been developed to detect MG due to its portability, rapid analysis, sensitivity, and low cost. Besides the detection of such pollutant, their degradation is also equally relevant and significant.

Heterogeneous photocatalysis is the best considered when conventional wastewater treatments using biological degradation, flocculation, adsorption, reverse osmosis, centrifugation are inefficient (Khan et al. 2024). Any heterogeneous photocatalytic reactions to occur must have at least three components (i) emitted photon energy from a source, (ii) a solid photocatalytic nanomaterial, and (iii) an oxidizing agent, preferably oxygen (Mondal et al. 2017). The dependency of using AuNPs in heterogeneous photocatalysis has been increased drastically due to its high optical absorption characteristics under both the visible and ultraviolet light irradiation and lower negative redox potential than bulk metallic gold (Zhang et al. 2022). Motivation from plasmonic AuNPs, a number of novels AuNPs/semiconductor photocatalyst have been designed to capture the visible energy, very specifically at their resonance frequencies at which they show high absorption and scattering cross-sections (Augustynski et al. 2016). The main objective behind the using of plasmonic AuNPs in photocatalysis is to enhance light absorption and subsequent photogeneration of charge carriers on semiconductor (Parente et al. 2018). The most widely used photocatalyst like TiO_2 and its derivative exhibits degradation property under UV radiation but eventually limited its application in the full range of solar energy (El-Khawaga et al. 2025). Unlike TiO_2, its AuNPs/nanocomposite can absorb visible light and act as an electron relay system between the reducing agent and the pollutant to facilitate the photodegradation or reduction phenomenon (Chansa et al. 2020).

In this paper, we demonstrate a green, facile and rapid method by combining a biosynthesis of AuNPs using *Citrus grandis* peel extract with the help of ultrasonic waves under ambient conditions. *Citrus grandis*; a tropical plant belongs to the family Rutaceae is a rich source of antioxidants like flavonoids (neohesperidin, hesperidin, naringin) and phenolic compounds, thus considering its use for biosynthesis of AuNPs (Nassarawa et al. 2024; Dheyab et al. 2025). The synthesized AuNPs was analytically characterized and evaluated for (i) electrocatalysis by analyzing the MG at AuNPs modified glassy carbon electrode (AuNPs/GCE), and (ii) photocatalysis by reducing the MG in presence of $NaBH_4$. To the best of our knowledge, no report has been documented on sono-assisted green synthesis of AuNPs using *C. grandis* and their dual catalytic performance towards MG.

Experimental

Chemical and reagents

Chloroauric acid ($HAuCl_4$) as a metal ion precursor, malachite green (MG) as a model dye, sodium

borohydride ($NaBH_4$) as a reducing agent, potassium ferrocyanide ($K_4[Fe(CN)_6].3H_2O$), potassium ferricyanide ($K_3[Fe(CN)_6]$), sodium dihydrogen phosphate (NaH_2PO_4), and di-sodium hydrogen phosphate (Na_2HPO_4), potassium chloride (KCl), and ethanol were procured from Sigma-Aldrich Chemicals, India and used as such. A 0.1 M PBS solution was prepared by mixing 0.1 M stock solutions of monopotassium dihydrogen phosphate (NaH_2PO_4) and dipotassium hydrogen phosphate (K_2HPO_4) with the pH adjusted to 5.0 by varying the ratio of the two components.

Preparation of *C. grandis* peel extract (CPE)

The *C. grandis* were collected from an agriculture farm in Chengalpattu, India. The peel was then cut into a small pieces, and thoroughly washed under running tap water followed by double-distilled water to remove the dust and organic impurities present on it and dried using the paper towel. Then, 25 g of dried peel was ground with 100 mL of sterilized Milli-Q water using morter and pastle and boiled for 15 min. The boiled extract was filtered through a nylon mesh, followed by Millipore hydrophilic filter (0.22 mm) and used for the experiments. Meanwhile the peel extract was stored in a refrigerator at 4 °C for all subsequent studies.

Biosynthesis of gold nanoparticles

Biogenic AuNPs was prepared by reducing $HAuCl_4$ under the influence of ultrasonic frequencies in the presence of peel extract. In a typical reaction procedure, 20 mL of 1 mM $HAuCl_4$ containing 20% (v/v) aqueous *C. grandis* peel extract (CPE) was exposed to varying intensity of ultrasonic irradiation (20, 40, 60 kHz, at 50 W) under ambient conditions for 5 min. The irradiation was carried out with a ultrasonic reactor (Branson Digital Sonifier-450, USA with a tip diameter of 10 mm) immersed directly into the reaction solution. Preliminary, the reduction of $AuCl_4^-$ ions to Au^0 were confirmed by monitoring the development of pink colour followed by the surface plasmon resonance (SPR) spectrum at 561 nm. Finally, the suspension was purified by repeated centrifugation at 10,000 rpm for 10 min and dried using a lyophilization for further studies. A control setup was also maintained without CPE extract.

Characterization of AuNPs

Characterization of biosynthesized AuNPs was extensively carried out using different analytical techniques. The bioreduction of Au^{3+} ions and progress of the reaction was monitored using a Perkin-Elmer double beam UV-vis spectrophotometer within 400–800 nm operated at a resolution of 1 nm in which water was used as blank. The topographical and morphological properties of the as-synthesized particles were analyzed by Field emission scanning electron microscopy (FESEM; FEI Quanta FEG 200) and Transmission electron microscopy (TEM; JEOL 1200 EX). The corresponding particle size distribution and surface charge of the AuNPs was determined using dynamic light scattering (DLS) coupled with zeta potential analyzer (Nanopartica SZ-100, Horiba Scientific). Crystalline metallic gold was examined by X-ray diffraction analysis (XRD; PANanalytical's X'pert X-ray diffractometer) with a Cu Kα radiation (λ = 0.15406 nm) for 2θ angles ranging from 10° to 90°. The diffractometer was operated at 40 kV, at room temperature with a scanning rate of 10°/min. The elemental composition of the nanomaterials was performed by Energy dispersive X-ray spectroscopy (EDX analyzer) equipped with FESEM instrument. To identify the possible biomolecules responsible for the reduction to the AuNPs were recorded by Fourier transform infrared spectroscopy (FTIR; Perkin-Elmer Spectrum-One FTIR spectrophotometer) within 400–4000 cm^{-1} at a resolution of 4 cm^{-1}. For that, the sample was centrifuged at 10,000 rpm for 10 min to obtain a solid at the bottom of the centrifuge tube. The solid was ground with KBr and pressed to obtain a pellet, which was used for FTIR analysis.

Fabrication of AuNPs/GCE

Prior to electrochemical modification, the bare GCE (3 mm in diameter) was cleaned and polished repeatedly with 1.0, 0.3, and 0.05 µM alumina/water slurries and mild sonicated with ethanol/water (3:1 v/v) for 2 min until shows mirrorlike surface. The electrode modification was carried out by a simple drop casting method. About 6 µL of colloidal AuNPs solution was uniformly cast onto the clean electrode and allowed to evaporate at room temperature. All electrochemical experiments were performed using a CH600Dsp+ electrochemical workstation consisting of conventional three electrode system with nano-gold decorated GCE as a working electrode, a platinum electrode as a counter electrode, and Ag/AgCl electrode as the reference electrode. The electrocatalytic behaviour of AuNPs/GCE was then examined using cyclic voltammetry (CV) in 5 mM of $[Fe(CN)_6]^{3-/4-}$ redox couple containing 0.1 M KCl at a scan rate of 50 mV s^{-1} for reversible electron transfer. The electrochemical detection of varying concentrations (1 to 40 µM) of MG in an acidic phosphate buffer solution (PBS) (pH ~ 5) was performed using DPV analysis within the potential of 0.3–1.2 V.

Photocatalytic reduction activity of biosynthesized AuNPs

To demonstrate the photocatalytic activity of the biosynthesized AuNPs, hydrogenated reduction of MG by $NaBH_4$ under visible light was considered as a model system. Briefly, 3 mL of 5×10^{-2} mol L^{-1} ice cold $NaBH_4$ solution was mixed with 10 mL of aqueous 9×10^{-5} mol L^{-1} MG solution in a screw cap vial. Followed by, 1 mL of colloidal AuNPs solution was added to this vial, thoroughly mixed, and exposed under direct sunlight. Prior to irradiation, the mixed solution was magnetically stirred in dark condition for 10 min. After a definite time of interval, the reduction of the dye was recorded in a UV-visible scanning spectrophotometer by monitoring the decrease of maxima absorbance corresponding to 616 nm until the solution becomes colourless and the corresponding percentage (%) of degradation was determined.

Results and discussion

Analytical characterization of biosynthesized AuNPs

The formation of AuNPs was confirmed by UV-visible scanning spectroscopy within 400 to 800 nm. The spectrum shows a signature SPR band appeared at approx. 561 nm due to coupling between the collective oscillation of the conduction electrons in resonance with irradiated electromagnetic radiation (Zhang et al. 2017; Ferdinand et al. 2021). Figure 1a represents the SPR spectrum of biogenic AuNPs at varying applied ultrasonic energy (20, 40, and 60 kHz, at 50 W) for 5 min in a solution of $HAuCl_4$ with CPE. Ocular speculation of the reaction revealed that the intensity of the change in colour from pale yellowish to ruby red increased with increasing the applied ultrasonic frequency. The SPR bands become broader and show a characteristic red shift with increasing the intensity of applied sonic waves indicates the formation of larger particles or aggregates. Such an observation is expected at higher sonic frequencies that cause secondary reduction process on the surface of preformed nuclei, giving rise to larger particles. Figure 1b represents the time kinetics of the biosynthesis reaction of AuNPs, where the intensity of the color changes rapidly with ultrasonic irradiation (40 kHz at 50 W) and reached maxima absorbance at 561 nm after 30 min.

While the SPR spectrum gives definite proof of the kinetics of AuNPs formation, the insight morphology, distribution and surface chemistry were examined using electron microscopy, DLS, and zeta potential analysis. FESEM micrograph represents the powder sample of biogenic AuNPs synthesized at 40 kHz, 50 W applied frequency for 5 min, as shown in Fig. 2(a). Most of the AuNPs are found to be aggregated and spherically shaped within diameter ranging from 30.7 to 49.3 nm. The surface of self-assembled dried nanoparticles is observed to be rough. The corresponding hydrodynamic diameter of the average AuNPs in the colloidal solution was determined by DLS and estimated to be 38.75 nm (inset of Fig. 2a), which is in accordance with FESEM analysis. While the TEM micrograph (Fig. 2b) of sonicated sample confirms the monodispersing nature of AuNPs. Direct observation of the image revealed that most of the grains were in spherical shape with only a few of them were triangular. It is also noticed that the AuNPs are coated with the biomoieties that might help to retain the definite spherical morphology. Inset of Fig. 2b reveals a negative electrokinetic zeta potential of -21.62 ± 0.08 mV at pH 7.4 due to the adsorption of biomolecules on the surface of AuNPs. This study indicates that AuNPs are stabilized by electrostatic repulsive forces. It was also observed that AuNPs were stable in the solution and showed very little aggregation even after 4 months. Hence, the phytoconstituents present in the *C. grandis* peel extract not only act as a reducing agent but also a capping agent to reduce the agglomeration of nanoparticles and help to control and stabilize the AuNPs (Ahmad et al. 2020).

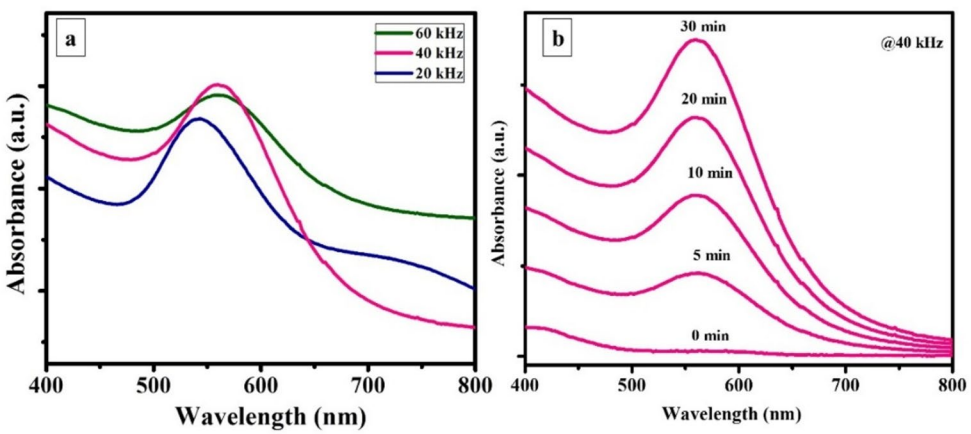

Fig. 1 **a** Exhibits absorption spectra of AuNPs synthesized at varying sono-energy (20, 40, and 60 kHz, 50 W) in presence CPE, and **b** time dependent SPR spectra of AuNPs at 40 kHz, 50 W

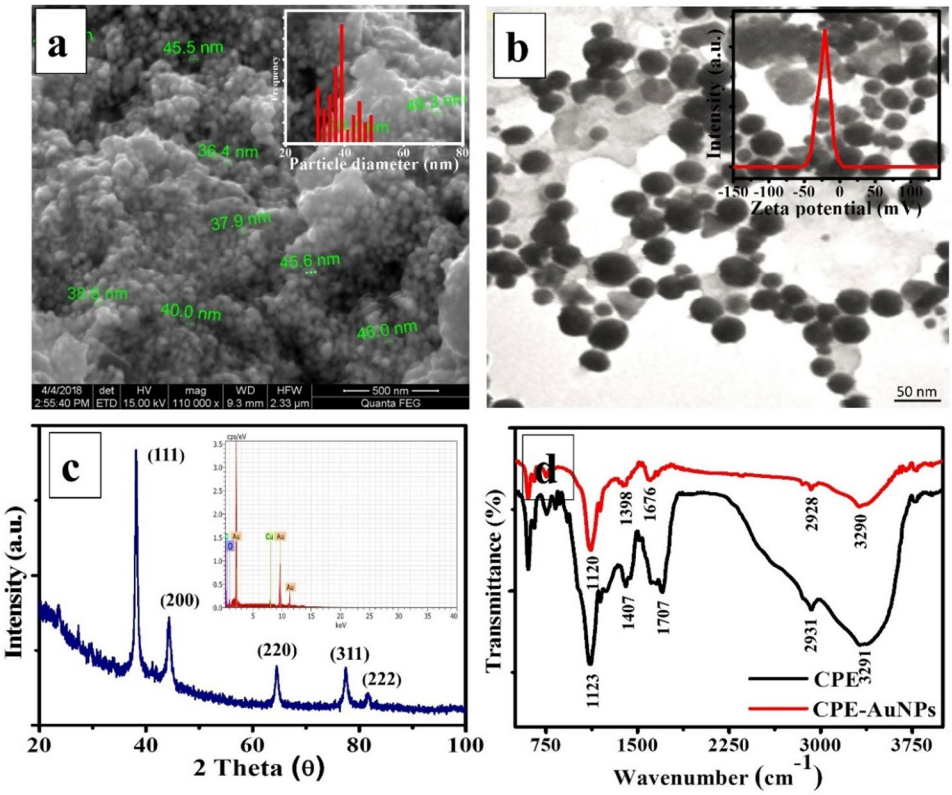

Fig. 2 Represents **a** FESEM, image of powdered AuNPs. Inset figure represents hydrodynamic distribution of particles; **b** TEM micrograph of spherically shaped AuNPs synthesized at 40 kHz, applied energy 50 W. Inset figure shows electrokinetic zeta potential of AuNPs; **c** XRD pattern of AuNPs. Inset figure represent EDX spectrum of the AuNPs; and **d** FTIR spectra of CPE and corresponding biosynthesized AuNPs

XRD analysis was carried out to determine the crystalline structure of AuNPs. Powder X-ray diffraction study was carried out to determine the crystalline structure and average size of the AuNPs. Figure 2c shows the sharp diffraction peaks at 2θ values of 38.23°, 44.65°, 64.78°, 77.56° and 81.97 corresponds to Bragg's reflection planes (1 1 1), (2 0 0), (2 2 0), (3 1 1) and (222), respectively. These lattice planes are indexed for face-centered cubic (fcc) phases (JCPDS No. 04-784) of crystalline gold (Mahakham et al. 2016). The intense Bragg reflection of (1 1 1) phase suggesting highly organized growth of the AuNPs. The mean diameter of the AuNPs was calculated using Debye–Scherrer's equation (Eq. 1) (Cao et al. 2020):

$$d = \frac{0.9\lambda}{\beta \cos\theta} \quad (1)$$

where d is the mean diameter of nanoparticles, β is the full width at half maximum (FWHM) of the XRD peak, λ is the wavelength of X-ray radiation source, θ is the diffraction angle, and determined to be 32.87 nm. Inset of Fig. 2c represents EDX profile of biogenic AuNPs, shows a sharp peak for elemental gold at 2 keV confirmed the bio-reduction of chloroauric acid to gold nanoparticles. The appearance of carbon (C) and oxygen (O) signals might correspond to the biomolecules adsorbed on the surface of AuNPs as a capping agent. In addition, a copper (Cu) peak was also noticed, which has originated from the Cu grid used for sample analysis.

In order to study the surface chemistry of the functional groups present onto the AuNPs, FTIR spectroscopy was performed. The remarkable shift in absorption bands to lower wavenumber depicts the coordination of metal and the plant metabolites. Figure 2d shows the FTIR spectrum of the lyophilized plant extract and the corresponding as-synthesized AuNPs. CPE showed characteristic bands at 1123, 1407, 1707, 2931, and 3291 cm^{-1} are indicating the complex biochemical nature of peel extract. The strong signal at 1123 and 1707 cm^{-1} are corresponding to the stretching vibration of C–OH bond of phenol, and C=O groups of an aromatic ring, respectively. The minor peak observed at 1407 and 2931 cm^{-1} may be attributed to –C–O– and symmetric stretching vibrations of C–H bond, respectively. In addition, a broad band located at 3291 cm^{-1} represents –O–H stretching vibrations, thereby indicating the presence of hydroxyl group (Emadi et al. 2017; Sampathkumar et al. 2020; Krishnan et al. 2016). While, biogenic AuNPs showed several bands located at 1120, 1398, 1676, 2928, and 3290 cm^{-1} with little changes in the position, suggesting that water-soluble phytoconstituents like flavonoids were involved in reduction process and stabilizing the AuNPs by surface layering the NPs to prevent them from agglomeration.

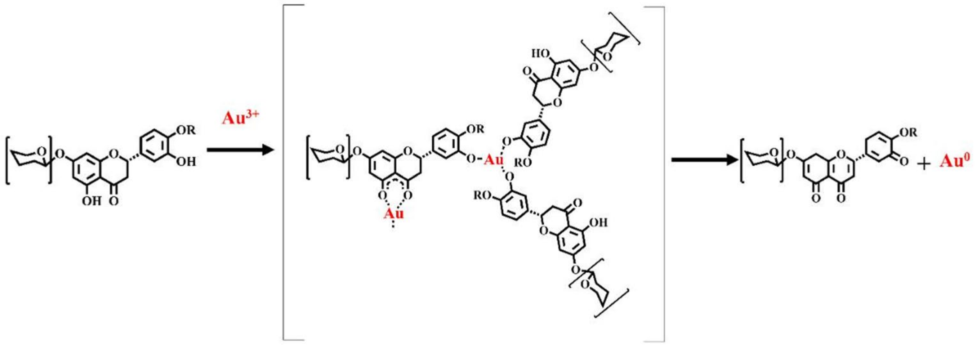

Fig. 3 Plausible mechanism of flavonoid mediated biosynthesis of AuNPs

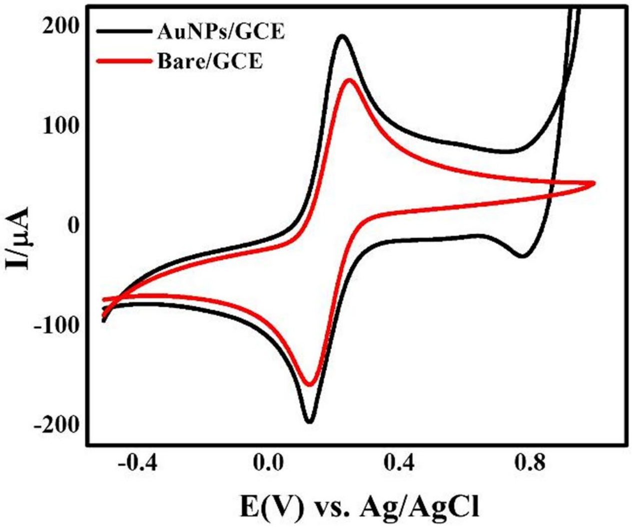

Fig. 4 Displays cyclic voltammogram of different modifications of the electrode (i) bare/GCE, and (ii) AuNPs/GCE in 5 mM of $[Fe(CN)]_6^{3-/4-}$

Literature study reported that CPE contain a high amount of water-soluble antioxidant polyphenols such as flavonoids (Zefang et al. 2016). These compounds possess ketonic (C=O) and hydroxyl (OH) groups, which can directly scavenge molecular species of active oxygen. The plausible chemistry for the formation of AuNPs has been illustrated in Fig. 3. It depicts that trivalent aurum (Au^{3+}) ions form an intermediate complex with flavonoids like naringenin through its hydroxyl (OH) groups. Then, the –OH groups undergo oxidation to its corresponding keto (C=O) forms and subsequently reduce the gold cation (Au^{3+}) to a neutral state of Au. The reduced Au^0 act as a nucleation site that undergoes agglomeration and eventually forms AuNPs (Oueslati et al. 2020).

Electrochemical study of AuNPs/GCE

In order to investigate the electrochemical performance, cyclic voltammetry (CVs) of the bare/GCE and AuNPs/GCE in 5 mM $[Fe(CN)]_6^{3-/4-}$ consisting 0.1 M KCl was considered as a probe reaction (Fig. 4). A couple of redox peaks were observed at bare/GCE with a peak-to-peak separation of 121 mV. The anodic and cathodic peak current response had been significantly intensified for AuNPs/GCE than bare/GCE, indicating the rapid electron transfer rate at the modified electrode. The enhanced electron transfer kinetics on the AuNPs/GCE might be attributed to the high conductivity and specific surface area of AuNPs. The electroactive surface area (A) of the modified electrode was determined from the anodic peak current ($I_{p.a.}$) of the CV in $[Fe(CN)]_6^{3-/4-}$ using the Randles-Sevcik equation (Eq. 2) for the reversible reaction (Mathew et al. 2018):

$$I_{pa} = 2.69 \times \ 10^5 n^{3/2} A D_0 C_0 \ ^{1/2} \tag{2}$$

where $I_{p.a.}$ is the anodic current response, n is the number of mobile electrons (1), ν is the scan rate (100 V s^{-1}), D_0 is the diffusion coefficient of the analyte (7.6 × 10^{-6} cm^2 s^{-1}), and C_0 is the concentration (5 mM). The effective surface area (A) at AuNPs/GCE was found to be 0.1617 cm^2.

The influence of varying scan rates (10 to 220 V s^{-1}) towards oxidation response of 10 mM MG at AuNPs/GCE was analysed using CV, and the sketch of superimposed voltammograms is shown in Fig. 5a. Figure 5b shows the corresponding linear relationship between anodic peak current ($I_{p.a.}$) and the square root of scan rate ($\nu^{1/2}$) and can be expressed as (Eq. (3)):

$$I_{pa} = \ -1.6551 \ + 5.1275 \times \ \ ^{1/2} \ (R^2 = 0.997) \tag{3}$$

which manifested the electrode reaction of MG at AuNPs/GCE as an irreversible process driven by adsorption. Further dealing with the data, a linear relationship between the peak potential ($E_{p.a.}$) and the logarithm of scan rate (logν) is demonstrated in Fig. 5c. The corresponding linear regression equation is expressed as Eq. (4) with a R^2 value of 0.99.

$$E_{pa} = \ 0.071 \times \ \log \ + 0.840 \tag{4}$$

According to Laviron's theory (Li et al. 2024), an irreversible electrode process can be demonstrated by the following equation (Eq. 5):

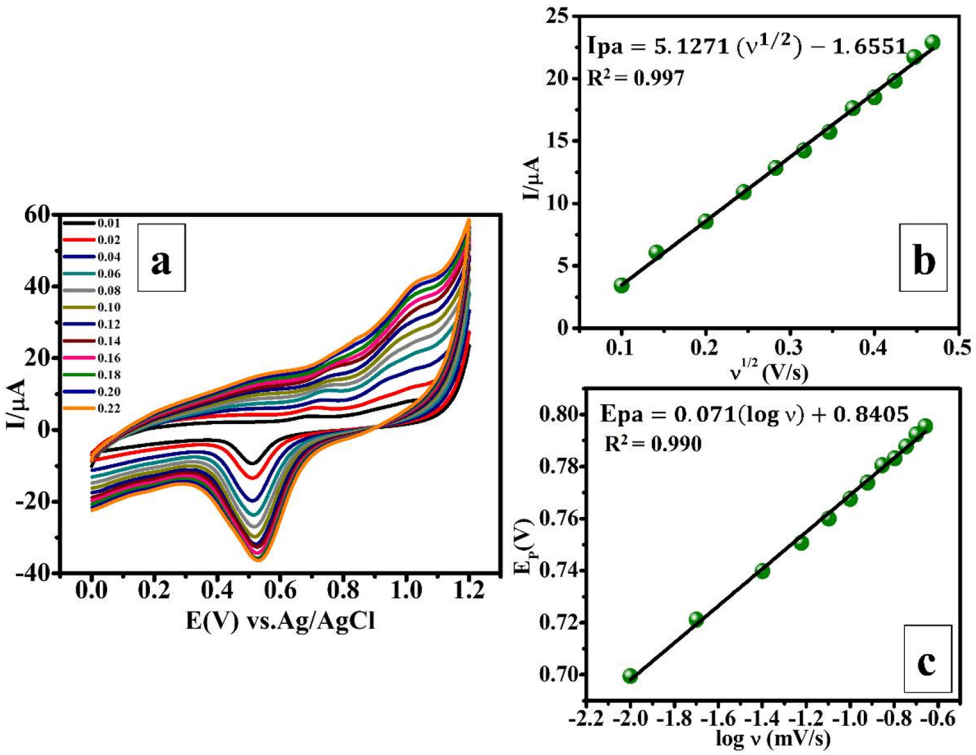

Fig. 5 **a** CVs of 100 mM MG at the AuNPs/GCE with different scan rates (10 to 220) V s^{-1}; **b** and **c** the corresponding calibration graph of I_p vs. $\nu^{1/2}$, and E_p vs. log ν, respectively

$$E_p\,(V) = E^0 - \frac{RT}{\alpha\, nF}\ln\frac{RTk_s}{\alpha\, nF} + \frac{RT}{\alpha\, nF}\ln \tag{5}$$

where E^0 is the formal standard potential, k_s is the standard heterogeneous rate constant, n is the number of electrons transferred, α refers to the charge transfer coefficient, ν, R, T and F have their usual significance. From the slope of Fig. 5c, the value of α was calculated to be 0.4164, considering the value of n is 2, as referred to in literature (Ansari and Nematollahi 2018). k_s can be obtained from the intercept of the E_p vs. log(ν) relationship until E^0 is known. E^0 was determined to be 0.718 V s^{-1} from the intercept of another linear relation of E_p vs. ν by extrapolating ν = 0. The value of k_s is estimated to be 0.27 s^{-1}. The diffusion coefficient (D_0) of the MG can be calculated using Randles-Sevcik's equation (Eq. (6) for the irreversible reaction (Bhattacharjee et al. 2024) and found to be 7.628×10^{-4} cm^2 s^{-1}.

$$I_{pa} = 2.99 \times 10^5\, nAC(\alpha\, nD)^{1/2} \tag{6}$$

Finally, differential pulse voltammetry (DPV) was employed for the quantitative detection of MG since the tool offers better sensitivity and resolving power. Sacara et al. previously documented that the electrochemical oxidation of MG in acidic media is two electron transferable irreversible reaction driven by diffusion control process at the electrode. During anodic oxidation reaction, MG eliminates its central C atom with a phenyl group to form an intermediate N, N,N′,N′-tetramethylbenzidine (TMB) which further oxidized to 1,1′-biphenyl-4.4′-diamine (TMB_{Ox}) (Sacara et al. 2017a, b). The anodic response corresponding to the electrooxidation of MG recorded in DPV was utilised to study the performance of the AuNPs modified electrodes. Figure 6a exhibits the DPV responses at AuNPs/GCE in the presence of varying concentrations (1, 2, 4, 6, 8, 10, 20, and 40 μM) of MG in acidic PBS (pH ~ 5) within the potential window of 0.3 to 1.2 V vs. Ag/AgCl/KCl_{sat}. The corresponding calibration plot shows the linear relationship between the concentration of MG and anodic peak currents ($I_{p.a.}$), as shown in Fig. 6b. The linear regression for the electrooxidation of MG is expressed as follows (Eq. 7):

$$I_{pa} = 0.0261 \times C_{MG} + 2.1071 (R2 = 0.9928) \tag{7}$$

The limit of detection (LoD) at AuNPs/GCE was calculated from LoD = 3σ/m at S/*N* = 3, where σ is the standard deviation of the blank response, and m is the slope of the calibrated graph. The estimated LoD at AuNPs/GCE is 298 nM with an apparent sensitivity of 0.373 μA μM^{-1} cm^{-2}.

In order to study the selectivity of the AuNPs/GCE, a number of interferents were introduced, including methylene blue, methyl orange, K_2SO_4 and NaCl which may cause interference during detection even present at low concentration compare to that of MG. For that, the sensor was incubated with 10 μM MG containing one of the above-mentioned interferents (0.1 M), respectively as demonstrated in the Fig. 6c where A is pure MG without any interferents,

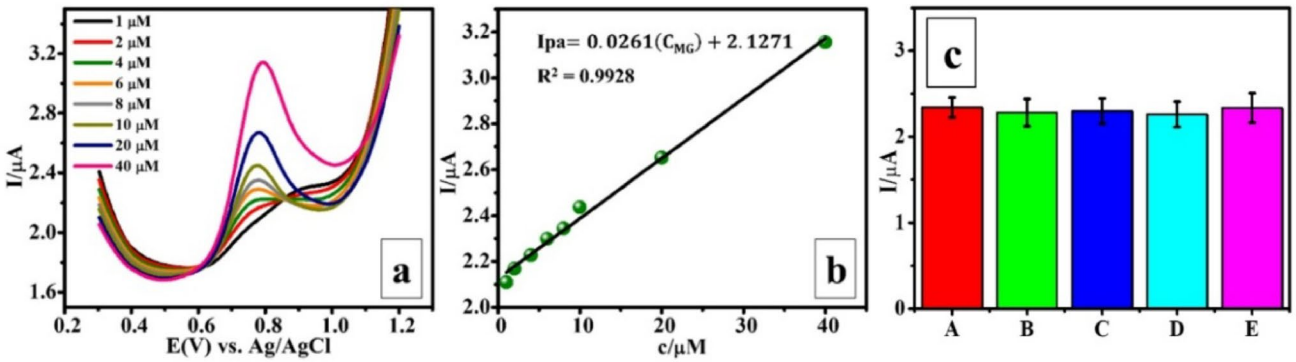

Fig. 6 Shows **a** DPV spectrum of different concentration of MG (1 to 40) µM at AuNPs/GCE in acidic PBS (pH ~ 5); **b** the corresponding calibration plot of the anodic peak current response ($I_{p.a.}$) vs. concentration of MG, and **c** specificity study towards various interfering agents where **A** is pure MG, and **B**, **C**, **D**, and **E** are mixture of MG and methylene blue, methyl orange, K_2SO_4 and, NaCl, respectively

and B, C, D, and E are mixture of MG and methylene blue, methyl orange, K_2SO_4 and NaCl, respectively. The change in current caused by the interferents was less than 5% compared to no interference, indicating that the sensor had good selectivity and these intereferents does not have any impact on MG detection. The reproducibility of the modified probe was also studied. The RSD for MG is found less than 5% for 5 independent electrodes under same experimental conditions. Together with good fabrication reproducibility, selectivity, and moderate dynamic range with LoD value suggest that AuNPs modified electrode for MG was quite reliable and can be further improved by conjugating with different conductive materials.

Photocatalytic reduction of MG

Catalysis is a typical nanoscale phenomenon, where nanomaterials are used to activate the chemical bonds of the intermediated substrate-product complexes to decrease the activation energy, which otherwise not. In order to realize the photocatalytic activity of biosynthesized AuNPs, the reduction of MG was performed by $NaBH_4$ under visible light irradiation as a probe reaction. Simultaneously it is observed that no change in maximum absorbance of MG at 616 nm in absence of AuNPs and $NaBH_4$ over the time indicates the no photolytic degradation of MG. Finally, the comparison of the photocatalytic behaviours of $NaBH_4$ with and without AuNPs was studied by recording the variation of maximum absorbance of MG at regular time intervals, as shown in Figs. 7(a and b). Figure 7a shows that without catalyst (AuNPs), the absorption maxima of MG decreases slowly with respect to time (approx. ~ 120 min) in the presence of $NaBH_4$. The intensity of the colour was also noticed to be fade than the control one indicates the ability of the $NaBH_4$ to reduce MG. While a rapid decrease in absorption maxima of MG is noticed after 39 min in the presence of AuNPs with $NaBH_4$ indicates the catalytic reduction of green coloured MG to colourless LMG (Fig. 7b). The rapid decrease of absorption maxima is indicative of the potential of AuNPs as a photocatalyst. The photo-induced reduction rate of MG was determined from the linear calibration plot of $\ln(A_t/A_0)$ vs. time (Fig. 7c). The apparent rate constant of the photocatalytic reduction of MG (κ_{app}) is estimated from the first-order kinetic equation (Eq. 8).

$$\ln\left(\frac{A_t}{A_0}\right) = -\kappa_{app}(t) \tag{8}$$

where A_t, A_0 indicates the absorbance at different time interval and initial time, respectively. A linear correlation was observed for the photocatalytic and non-catalytic reaction between $\ln(A_t/A_0)$ vs. time, which follows first-order kinetics as expressed in Eqs. (9 and 10), respectively.

$$\ln\left(\frac{A_t}{A_0}\right) = -0.0451\,(t) + 0.0689 \; R^2 = \; 0.9886 \tag{9}$$

$$\ln\left(\frac{A_t}{A_0}\right) = -0.0096\,(t) + 0.0265 \; R^2 = \; 0.9961 \tag{10}$$

The κ_{app} for the photocatalytic reaction is estimated to be 4.51×10^{-2} min^{-1} as compared to 0.96×10^{-2} min^{-1} for non-catalytic reaction. This result confirms the rapid and effective photocatalytic reduction of MG by AuNPs. The percentage (%) of dye degradation for catalytic reaction was calculated from Eq. (11) and plotted against time (Fig. 7d).

$$\%\text{ of dye degradation} = \left(\frac{A_0 - A_t}{A_0}\right) \times \; 100 \tag{11}$$

The plot clearly demonstrates that the biogenic AuNPs was an effective catalyst against MG and the maximum percentage (%) of degradation was achieved at 81.93% after 39 min.

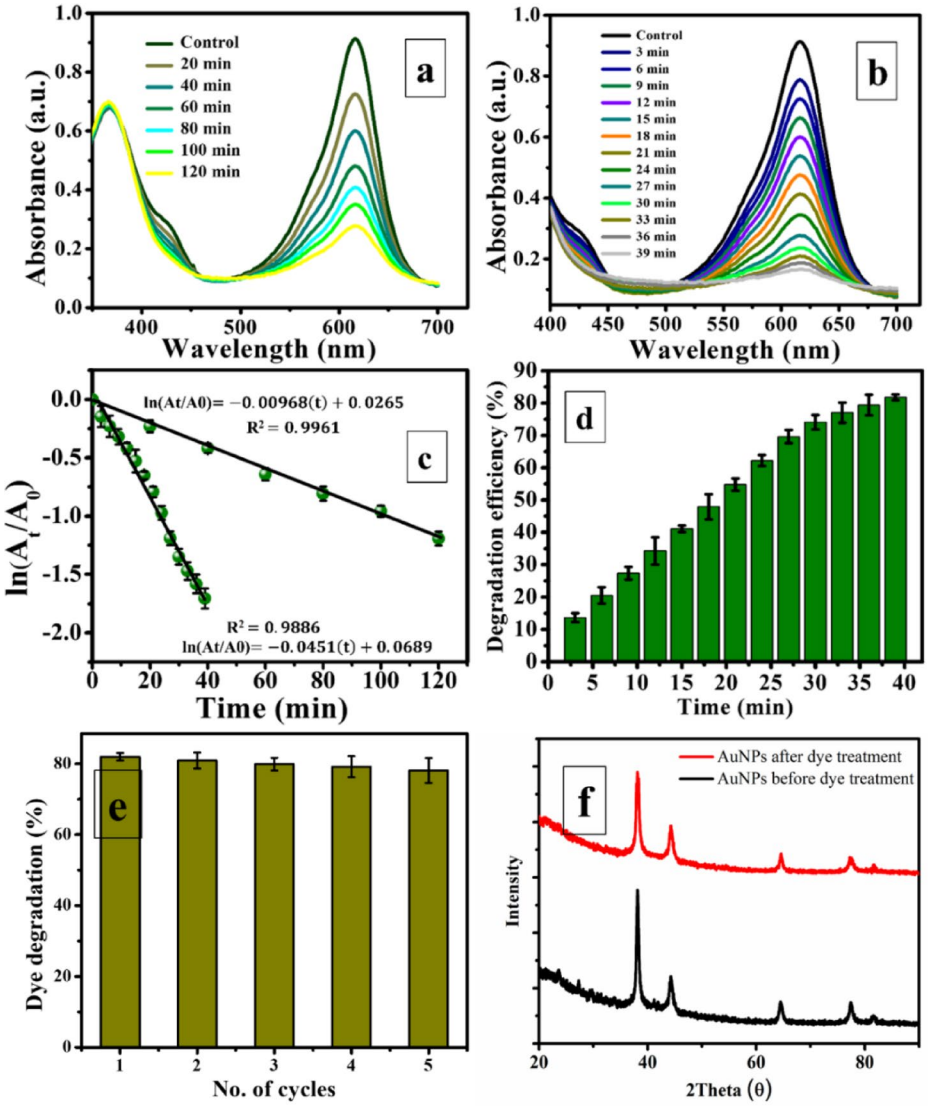

Fig. 7 Exhibits **a** time-dependent UV–visible spectra of degradation of MG in absence of AuNPs under the visible light irradiation with $NaBH_4$; **b** time-dependent UV-visible spectra of photocatalytic degradation of MG in presence of AuNPs under the visible light irradiation with $NaBH_4$; **c** the corresponding calibration plot of $\ln(A_t/A_0)$ vs. time for uncatalyzed and catalyzed reaction; **d** the corresponding calibration plot of time vs. percentage (%) of dye degradation; **e** reusability of photocatalyst (AuNPs) for MG degradation under visible light illumination; and **f** XRD profiles of AuNPs before and after treatment of dye

The AuNPs catalysed photodegradation of MG in presence of $NaBH_4$ is considered as a heterogeneous catalytic reaction. The photocatalytic efficiency of AuNPs is clarified through the reductive mechanism and pictorially illustrated in Fig. 8. The complete photocatalytic dye reduction involves three sequential steps. (A) Diffusion and adsorption of borohydride ions (e^- donor) and MG (e^- acceptor) onto the surface of photocatalyst (AuNPs). (B) Transfer of electrons between them. Briefly, the electron transfer mechanism is as follows. (i) AuNPs absorbs visible light (sunlight) strongly because the surface plasmon oscillation frequency for AuNPs is in the visible spectrum. The corresponding photon energy (hv) is sufficient to overcome the attraction forces of the electrons from the nucleus of AuNPs (Eg ~ 2.21 eV) and causes the excitation of electrons from the low energy filled valence band (VB) to the high energy empty conduction band (CB). Thereby resulting formation of a positively charged hole (h^+) in the valence band and a negatively charged free electron (e^-) in the conduction band or electron-hole (e^-/h^+) pair separation. (ii) The e^-/h^+ pairs can migrate to the surface of AuNPs and be involved in oxidation and reduction reactions. (iii) The electron in CB reacts with toxic MG and reduced to non-toxic LMG, and (iv) simultaneously, the hole in VB interacts with $NaBH_4$ and oxidized to $NaBO_2$. (C) LMG and $NaBO_2$ diffuse away from the surface of photocatalyst. Herein, $NaBH_4$ in the presence of visible light is facilitating the insertion of an electron into empty VB and subsequently migrate them into CB of the AuNPs, and followed by reduction of dye on the surface of AuNPs. Hence, AuNPs as a photocatalyst is an essential for electron relay effect from $NaBH_4$ to the dye for the dye reduction process (Zhao and Jin 2018; Bhowmik et al. 2015; Zhang et al. 2025; Singh et al. 2020; Sonu et al. 2019).

Finally, to investigate the reusability of the AuNPs as photocatalyst, five successive degradation reaction of MG

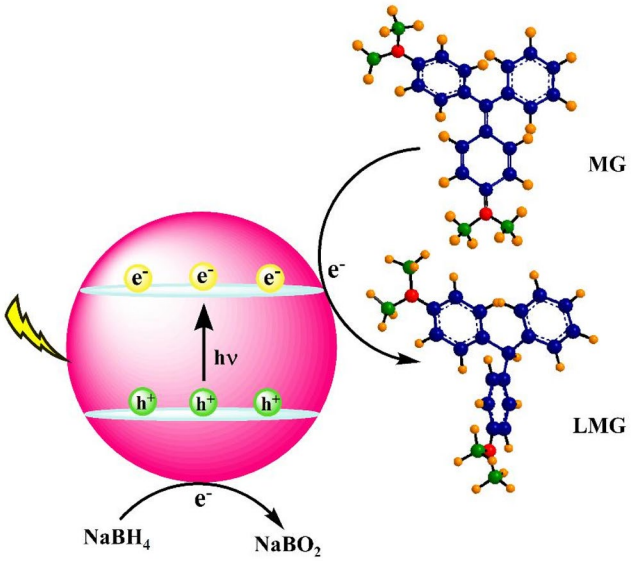

Fig. 8 Plausible mechanism of photocatalytic degradation of MG in presence of $NaBH_4$ with AuNPs under the visible light irradiation

under visible light illumination was performed in the same experimental condition. As shown in Fig. 7e, the degradation efficiency of the photocatalyst was observed insignificant or slightly reduced from 81.93% (1st cycle) to 78.06% (5th cycle), reflects the stability of the photocatalyst. Moreover, the XRD pattern (Fig. 7f) of the reused photocatalyst did not exhibit any notable changes in its crystalline structure suggests that the as-synthesized AuNPs can be used as a reusable photocatalyst for degradation of MG.

Conclusion

In summary, we have successfully demonstrated a rapid and feasible green chemistry synthesis for AuNPs using *C. grandis* peel extract as reducing and stabilizing agent assisted by ultrasonic waves. The particles are found crystalline and predominantly spherically shape with little aggregation as evidenced from XRD, FESEM and TEM, respectively. The as-synthesized AuNPs was investigated for electrocatalysis and showed a moderately broad dynamic range with a limit of detection (LoD) of 298 nM for MG. Besides, as an electrocatalyst, the AuNPs possessed photocatalytic activity towards degradation of MG with an apparent rate constant value of 4.51×10^{-2} min^{-1}. So, this piece of work concludes that ultrasound-mediated biogenic AuNPs is a potential bifunctional catalyst could stimulate future applications in biomedical as well as in wastewater management.

Acknowledgements We gratefully acknowledge Department of Biotechnology, School of Bioengineering, SRMIST for providing electrochemical workstation and lab space to carry out this research.

Declarations

Conflict of interest There is no conflict of interest to declare.

References

Ahmad T, Bustam MA, Zulfiqar M, Moniruzzaman M, Idris A, Iqbal J, Asghar HMA, Ullah S (2020) Controllable phytosynthesis of gold nanoparticles and investigation of their size and morphology-dependent photocatalytic activity under visible light. J Photochem Photobiol A 392:112429

Ahmad A, Mushtaq Z, Saeed F, Afzaal M, Jbawi EA (2023) Ultrasonic-assisted green synthesis of silver nanoparticles through cinnamon extract: biochemical, structural, and antimicrobial properties. Int J Food Prop 26:1984–1994

Ansari A, Nematollahi D (2018) A comprehensive study on the electrocatalytic degradation, electrochemical behavior and degradation mechanism of malachite green using electrodeposited nanostructured β-PbO_2 electrodes. Water Res 144:462–473

Augustynski J, Bienkowski K, Solarska R (2016) Plasmon resonance-enhanced photoelectrodes and photocatalysts. Coord Chem Rev 325:116–124

Bhattacharjee S, Neppolian B, Das J (2024) Electrochemical fabrication of AuPt nanoalloy embedded nitrogen-doped reduced graphene oxide (AuPt@N-erGO) based combinatorial dual-analyte sensor. J Alloys Compd 1004:175712

Bhosale MA, Chenna DR, Bhanage BM (2017) Ultrasound assisted synthesis of gold nanoparticles as an efficient catalyst for reduction of various nitro compounds. ChemistrySelect 2:1225–1231

Bhowmik T, Kundu MK, Barman S (2015) Ultra small gold nanoparticles–graphitic carbon nitride composite: an efficient catalyst for ultrafast reduction of 4-nitrophenol and removal of organic dyes from water. RSC Adv 5:38760–38773

Cao Y, Zhou G, Zhou R, Wang C, Chi B, Wang Y, Hua C, Qiu J, Jin Y, Wu S (2020) Green synthesis of reusable multifunctional γ-Fe_2O_3/bentonite modified by doped TiO_2 hollow spherical nanocomposite for removal of BPA. Sci Total Environ 708:134669

Chansa JL, Wewers F, Mthethwa T (2020) Plasmonic photocatalysts consisting of a mixture of Au nanospheres and Au nanorods on TiO_2 support for improved visible light induced photocatalytic degradation properties. J Photochem Photobiol B 401:112740

Choudhary BC, Paul D, Gupta T, Sandesh R, Tetgure SR, Garole VJ, Borse AU, Garole DJ (2017) Photocatalytic reduction of organic pollutant under visible light by green route synthesized gold nanoparticles. J Environ Sci 55:236–246

Das J, Velusamy P (2014) Catalytic reduction of methylene blue using biogenic gold nanoparticles from *Sesbania grandiflora* L. J Taiwan Inst Chem E 45(5):2280–2285

Deshmukh AR, Gupta A, Kim BS (2019) Ultrasound assisted green synthesis of silver and iron oxide nanoparticles using fenugreek seed extract and their enhanced antibacterial and antioxidant activities. BioMed Res Int 2019:1714358

Dheyab MA, Abdullah W, Aziz AA, Alanezi ST, Oladzadabbasabadi N, Khaniabadi PM, Jameel MS, Braim FS, Al-Jawarneh MA, Mohammad AIJM, Rahman AA, Mehrdel B (2025) Mechanistic insights and advances in polyphenol- and flavonoid-mediated sustainable synthesis of gold nanoparticles from agricultural waste: A review. Int J Biol Macromol 320:145978

Dinesh GK, Pramod M, Chakma S (2020) Sonochemical synthesis of amphoteric Cu^0-nanoparticles using *Hibiscus rosa-sinensis* extract and their applications for degradation of 5-fluorouracil and lovastatin drugs. J Hazard Mater 399:123035

El-Khawaga AM, Elsaidy A, Correa-Duarte MA, Elbasuney S (2025) Unveiling the photocatalytic and antimicrobial activities of star–shaped gold nanoparticles under visible spectrum. Sci Rep 15:1201

Elsupikhe RF, Shameli K, Ahmad MB (2015) Effect of ultrasonic radiation's times to the control size of silver nanoparticles in κ-carrageenan. Res Chem Intermed 41:8829–8838

Emadi F, Amini A, Gholami A, Ghasemi Y (2017) Functionalized graphene oxide with chitosan for protein nanocarriers to protect against enzymatic cleavage and retain collagenase activity. Sci Rep 7:42258

Ferdinand AC, Manikandan D, Manikandan P, Kavitha G, Gaur R, Maaza M, Manikandan E (2021) Nobel Ag–Cu ion-exchange bimetallic nanoclusters formation over gold ion (Au^{2+}) implanted materials RBS and optical study. Radiat Eff Defects Solids 176(9–10):955–966

Franco-Romano M, Gil MLA, Palacios-Santander JM, Delgado-Jaén JJ, Naranjo-Rodríguez I, de Cisneros JLH-H, Cubillana-Aguilera LM (2014) Sonosynthesis of gold nanoparticles from a geranium leaf extract. Ultrason Sonochem 21:1570–1577

Jameel MS, Aziz AA, Dheyab MA (2020) Comparative analysis of platinum nanoparticles synthesized using sonochemical-assisted and conventional green methods. Nano-Struct Nano-Objects 23:100484

Karadirek S, Okkay H (2019) Ultrasound assisted green synthesis of silver nanoparticle attached activated carbon for levofloxacin adsorption. J Taiwan Ins Chem Eng 105:39–49

Khan S, Noor T, Iqbal N, Yaqoob L (2024) Photocatalytic Dye Degradation from Textile Wastewater: A Review. ACS Omega 9:21751–21767

Krishnan V, Bupesh G, Manikandan E, Arul KT, Magesh S, Kalyanaraman R, Maaza M (2016) Green synthesis of silver nanoparticles using *Piper nigrum* concoction and its anticancer activity against MCF-7 and Hep-2 cell lines. J Antimicro 2:123

Kumar SV, Bafana AP, Pawar P, Rahman A, Dahoumane SA, Jeffrye CS (2018) High conversion synthesis of < 10 nm starch-stabilized silver nanoparticles using microwave technology. Sci Rep 8:5106

Li Y-Y, Chen Y-J, Abdalsadeg SAM, Xu K-X, Ma L-L, Moosavi-Movahedi AA, Hong J, Xiao B-L (2024) Biosensor based on ZIF-67-HRP and MWCNTs nanocomposite modified glass carbon electrode for the detection of luteolin in vegetable. Langmuir 40:20495–20504

Mahakham W, Theerakulpisut P, Maensiri S, Phumying S, Sarmah AK (2016) Environmentally benign synthesis of phytochemicals-capped gold nanoparticles as nanopriming agent for promoting maize seed germination. Sci Total Environ 573:1089–1102

Mathew G, Dey P, Das R, Chowdhury SD, Das MP, Veluswamy P, Neppolian B, Das J (2018) Direct electrochemical reduction of hematite decorated graphene oxide (α-Fe_2O_3@erGO) nanocomposite for selective detection of Parkinson's disease biomarker. Biosens Bioelectron 115:53–60

Mondal S, Reyes MEDA, Pal U (2017) Plasmon induced enhanced photocatalytic activity of gold loaded hydroxyapatite nanoparticles for methylene blue degradation under visible light. RSC Adv 7:8633–8645

Nasef MM, Zakeri M, Asadi J, Abouzari-Lotf E, Ahmad A, Malakooti R (2016) Environmentally benign and highly regios-elective ring opening of epoxides accelerated by ultrasound irradiation. Green Chem Lett Rev 9:76–84

Nassarawa SS, Dandago MA, Yusuf HL, Gambo A, Sanusi NI, Bako HK, Sulaiman SA, Mohammed M, Garba U (2024) Pharmacological properties of citrus fruit. In: Gupta AK, Kour J, Mishra P. (eds) Citrus Fruits and Juice. Springer, Singapore.109–132

Nojedehi ME, Malmiri HJ, Shahrouzi JR (2018) Hydrothermal green synthesis of gold nanoparticles using mushroom (*Agaricus bisporus*) extract: physico-chemical characteristics and antifungal activity studies. Green Process Synth 7:38–47

Oueslati MH, Tahar LB, Harrath AH (2020) Catalytic, antioxidant and anticancer activities of gold nanoparticles synthesized by kaempferol glucoside from Lotus leguminosae. Arab J Chem 13:3112–3122

Parente M, Sheikholeslami S, Naik GV, Dionne JA, Baldi A (2018) Equilibration of photogenerated charge carriers in plasmonic core@shell nanoparticles. J Phys Chem C 122(41):23631–23638

Patil AB, Bhanage BM (2016) Sonochemistry: A greener protocol for nanoparticles synthesis. In: Aliofkhazraei M (ed) Handbook of Nanoparticles. Springer Cham, pp 143–166

Poklepovich-Caride S, Oestreicher V, Zalduendo MM, Bordoni AV, Soler-Illia GJAA, Angelomé PC (2022) A versatile one-pot room temperature approach for the synthesis of gold nanoparticles with multiple sizes and shapes. Colloids Surf A: Physicochem Eng Asp 645:128890

Sacara AM, Cristea C, Muresan LM (2017a) Electrochemical detection of Malachite Green using glassy carbon electrodes modified with CeO_2 nanoparticles and nafion. J Electroanal Chem 792:23–30

Sacara AM, Nairi V, Salis A, Turdean GL, Muresan LM (2017b) Silica-modified electrodes for electrochemical detection of malachite green. Electroanalysis 29(11):2602–2609

Sáez V, Mason TJ (2009) Sonoelectrochemical synthesis of nanoparticles. Molecules 14:4284–4299

Sampathkumar Y, Elumalai S, Manikandan E, Priya M (2020) Biogenic Silver Nanoparticles /Clusters Synthesis Characterization by Scanning Electron Microscopy and 2D-3D Topographical Analysis by Mountain -®- graphical tool. J Nanomed Nanotechnol 11:556

Satpathy G, Manikandan E (2020) Nanoparticles and their application as antibacterial tool. Solid State Technol 63:2724–2731

Shirazi FS, Akhbar K (2016) Sonochemical procedures; the main synthetic method for synthesis of coinage metal ion supramolecular polymer nano structures. Ultrason Sonochem 31:51–61

Singh P, Shandilya P, Raizada P, Sudhaik A, Rahmani-Sani A, Hosseini-Bandegharaei A (2020) Review on various strategies for enhancing photocatalytic activity of graphene based nanocomposites for water purification. Arab J Chem 13:3498–3520

Sonu DV, Sharma S, Raizada P, Hosseini-Bandegharaei A, Gupta VK, Singh P (2019) Review on augmentation in photocatalytic activity of $CoFe_2O_4$ via heterojunction formation for photocatalysis of organic pollutants in water. J Saudi Chem Soc 23:1119–1136

Usman AI, Aziz AA, Khaniabadi PM (2020) Sonochemical synthesis of gold nanoparticles via palm oil fronds extracts for cytotoxicity assay. Mater Sci Eng 839:012004

Vasantharaj S, Sripriya N, Shanmugavel M, Manikandan E, Gnanamani A, Senthilkumar P (2018) Surface active gold nanoparticles biosynthesis by new approach for bionanocatalytic activity. J Photochem Photobiol B 179:119–125

Vergis BR, Hari Krishna R, Kottam N, Nagabhushana BM, Sharath R, Darukaprasad B (2018) Removal of malachite green from aqueous solution by magnetic $CuFe_2O_4$ nano-adsorbent synthesized by one pot solution combustion method. J Nanostruct Chem 8:1–12

Wan H, Li C, Mahmud S, Liu H (2021) Kappa carrageenan reduced-stabilized colloidal silver nanoparticles for the degradation of toxic azo compounds. Colloids Surf Physicochem Eng Asp 616:126325

Zefang L, Zhao Z, Hongmei W, Zhiqin Z, Jie Y (2016) Phenolic composition and antioxidant capacities of chinese local pummelo cultivars' peel. Hortic Plant J 2(3):133–140

Zhang R, Bursi L, Cox JD, Cui Y, Krauter CM, Alabastri A, Manjavacas A, Calzolari A, Corni S, Molinari E, Carter EA, Abajo JFGD, Zhang H, Nordlander P (2017) How to identify plasmons from the optical response of nanostructures. ACS Nano 11:7321–7335

Zhang J, Huang Z, Xie Y, Jiang X (2022) Modulating the catalytic activity of gold nanoparticles using amine-terminated ligands. Chem Sci 13:1080–1087

Zhang P, Hou H, Xu S, Wen Y, Zhang Y, Xing F (2025) Localized surface plasmon resonance sensing based on monometallic gold nanoparticles: from material preparation to detection of bioanalytes. Anal Methods 17:892–915

Zhao J, Jin R (2018) Heterogeneous catalysis by gold and gold-based bimetal nanoclusters. Nano Today 18:86–102